Space charge governs the kinetics of metal exsolution

Moritz L. Weber [1, 2, 3, 4,*], Břetislav Šmíd [5], Uwe Breuer [6], Marc-André Rose [1, 3, 7], Norbert H. Menzler [2, 4], Regina Dittmann [1, 3], Rainer Waser [1, 3, 7], Olivier Guillon [2, 4, 8], Felix Gunkel [1, 3,*] and Christian Lenser [2,*]

1 Peter Gruenberg Institute - Electronic Materials (PGI-7), Forschungszentrum Juelich GmbH, 52425 Juelich, Germany
2 Institute of Energy and Climate Research – Materials Synthesis and Processing (IEK-1), Forschungszentrum Juelich GmbH, 52425 Juelich, Germany
3 Juelich-Aachen Research Alliance (JARA-FIT), 52425 Juelich, Germany
4 Institute of Mineral Engineering (GHI), RWTH Aachen University, 52062 Aachen, Germany
5 Department of Surface and Plasma Science, Charles University, 18000 Prague, Czech Republic
6 Central Institute for Engineering, Electronics and Analytics (ZEA-3), Forschungszentrum Juelich GmbH, 52425
7 Institute for Electronic Materials (IWE 2), RWTH Aachen University, 52074 Aachen, Germany
8 Juelich-Aachen Research Alliance (JARA-Energy), 52425 Juelich, Germany

ABSTRACT

Nanostructured composite electrode materials play a major role in the field of catalysis and electrochemistry. Self-assembly of metallic nanoparticles on oxide supports *via* metal exsolution relies on the transport of reducible dopants towards the perovskite surface to provide accessible catalytic centers at the solid/gas interface. However, it is unclear if exsolution can be driven from the oxide bulk or if the process is limited to surfaces and interfaces, where strong electrostatic gradients and space charges typically control the properties of oxides. Here we reveal that the nature of the surface-dopant interaction is the main determining factor for the exsolution kinetics of nickel in $SrTi_{0.9}Nb_{0.05}Ni_{0.05}O_{3-\delta}$ and that the exsolution depth is strongly limited to the near-surface region of the perovskite oxide. Electrostatic interaction of dopants with surface space charge regions forming upon thermal annealing result in strong surface passivation *i.e.* a retarded exsolution response. We furthermore demonstrate the controllability of the exsolution response *via* engineering of the perovskite surface chemistry. Our findings indicate that tailoring the electrostatic gradients at the perovskite surface is an essential step to improve exsolution-type materials in catalytic converters.

INTRODUCTION

Innovative concepts for the design of active and stable catalysts can enable key technologies to buffer the intermittency of renewable energy technologies or to produce green hydrogen, using (electro)chemical energy conversion devices such as electrolyzers and fuel cells, catalytic membrane reactors or heterogeneous catalysis.[1–4] Here, nanocomposites play a crucial role for the development of high-performance energy materials. Metal exsolution processes promise manifold benefits in comparison to conventional methods for the preparation of supported nanoparticles, such as *in-situ* activation and catalyst regeneration by reversible cycling of the process, and have received a growing interest in the field of energy materials.[5–13] Perovskite oxides doped with reducible transition metal cations serve as parent compounds for the fabrication of self-assembled, uniformly distributed and highly dispersed metallic nanoparticles on oxide supports.

A simple reducing treatment is applied to induce the growth of nanoparticles at the perovskite surface, which are formed from dopant cations. Despite the simplicity of nanocomposite synthesis *via* the exsolution route, the mechanisms that underpin the metal exsolution process have yet to be resolved and are controversially discussed within the field. The nucleation of metallic nanoparticles is driven by the change in Gibbs free energy ΔG associated with the transition from the respective metal oxide to the metallic state at low oxygen partial pressure.[5,14,15] However, the transport of dopants towards the surface requires a physical or chemical gradient to favour their emergence at the oxide surface rather than in the bulk. Here, the observation of subsurface nanoparticle nucleation has fueled the debate about the transport of extended metallic particles through the surrounding oxide host lattice.[8,16,17] In this model, the elastic strain energy at the interface between the embedded particles and the host lattice as well as the minimization of the surface free energy is considered to drive the release of nanoparticles to the surface. On the contrary, classical defect chemistry concepts are often applied to explain the exsolution behaviour by diffusive ionic movement.[7,15,18]

The mechanistic processes involved in dopant transport are likely to determine the time and length scales metal exsolution processes take place on, which is an open question in the field.[10] Although the surface properties of functional oxides are widely mediated by space charge and are known to dictate the ionic mass transport in many functional oxides[19–34], it has been neglected entirely in the proposed transport mechanisms of exsolution. Hence, the interaction of the exsolving species with the energy- and electrostatic field landscape at the surface remains unexplored.

Here we present experimental evidence that space charge regions formed at the perovskite surface during thermal annealing play a critical role for the exsolution kinetics. Our findings offer important insights into the fundamental processes involved in the formation of exsolution nanoparticles at oxide surfaces, based on a systematic comparison of the redox response of $SrTi_{0.9}Nb_{0.05}Ni_{0.05}O_{3-\delta}$ thin films in oxidizing and reducing conditions. Epitaxial thin films serve as model systems for the surfaces of single powder grains of typical exsolution materials. We furthermore demonstrate that the exsolution behaviour can be modified by tailoring the redox chemistry of the topmost surface region of the material. Please note that, throughout our discussion, the term *exsolution* primarily refers to the formation of nanoparticles at the solid/gas interface, most relevant for the functionality of exsolution-type catalysts, while exsolution of buried metallic nanoparticles proceeds under reducing thermal treatment across the entire oxide thin film.[17]

RESULTS

Surface limitations of the exsolution response

The exsolution response of nickel is studied based on well-defined (001)-oriented $SrTi_{0.9}Nb_{0.05}Ni_{0.05}O_{3-\delta}$ (STNNi) epitaxial thin films (*cf.* Supplementary Information (SI), Supplementary Fig. S1). This approach mimics the surfaces of exsolution-active perovskite materials on a single grain level, while at the same

time providing atomically smooth perovskite surfaces and well-defined probing geometries.[16] After reducing thermal treatment, finely structured decorations are visible at the crystal surface (Fig. 1a). Depending on the applied temperature, a variation in the nanoparticle density and the nanoparticle dimensions is evident (Fig. 1b, left panel). Interestingly, however, there is no statistically significant difference in the total volume of all nanoparticles after reduction at different temperatures (Fig. 1b, right panel). Instead, our findings indicate the nucleation and subsequent Ostwald ripening of a fixed volume of Ni on the surface. If metal exsolution is considered to be driven by the material striving towards thermodynamic equilibrium and to be based on bulk defect-chemical reactions, the amount of exsolved metal would be expected to be temperature dependent. High temperatures should result in accelerated mass transport and thus a stronger exsolution response that manifests in a larger total volume of exsolved Ni present at the perovskite surface.

To evaluate the concentration profile of nickel within the thin film after exsolution, depth-profiling by secondary ion mass spectrometry (SIMS) is applied after capping the thin films with platinum to avoid initial sputtering artefacts. Crossing the platinum-to-STNNi interface, a delay between the increase of the Ni-signal and the signal of the host cations (Sr, Ti) as well as Nb-dopants becomes apparent (Fig. 1c). The early increase of the Ni-signal corresponds to the accumulation of nickel at the surface, which is an indicator of Ni exsolution. The accumulation width can be estimated to be of the order of the nanoparticle height (approximately ~2 nm) using the thin film thickness as internal reference. However, no significant changes in the Ni-distribution across the thickness of the thin film are visible in comparison to the as-prepared sample (Supplementary Fig. S2). In particular, no depletion of Ni in the film and no gradient in the Ni content is detected by SIMS. Likewise, no significant differences in the accumulation width were detected by SIMS after reduction at different temperatures (Supplementary Fig. S2).

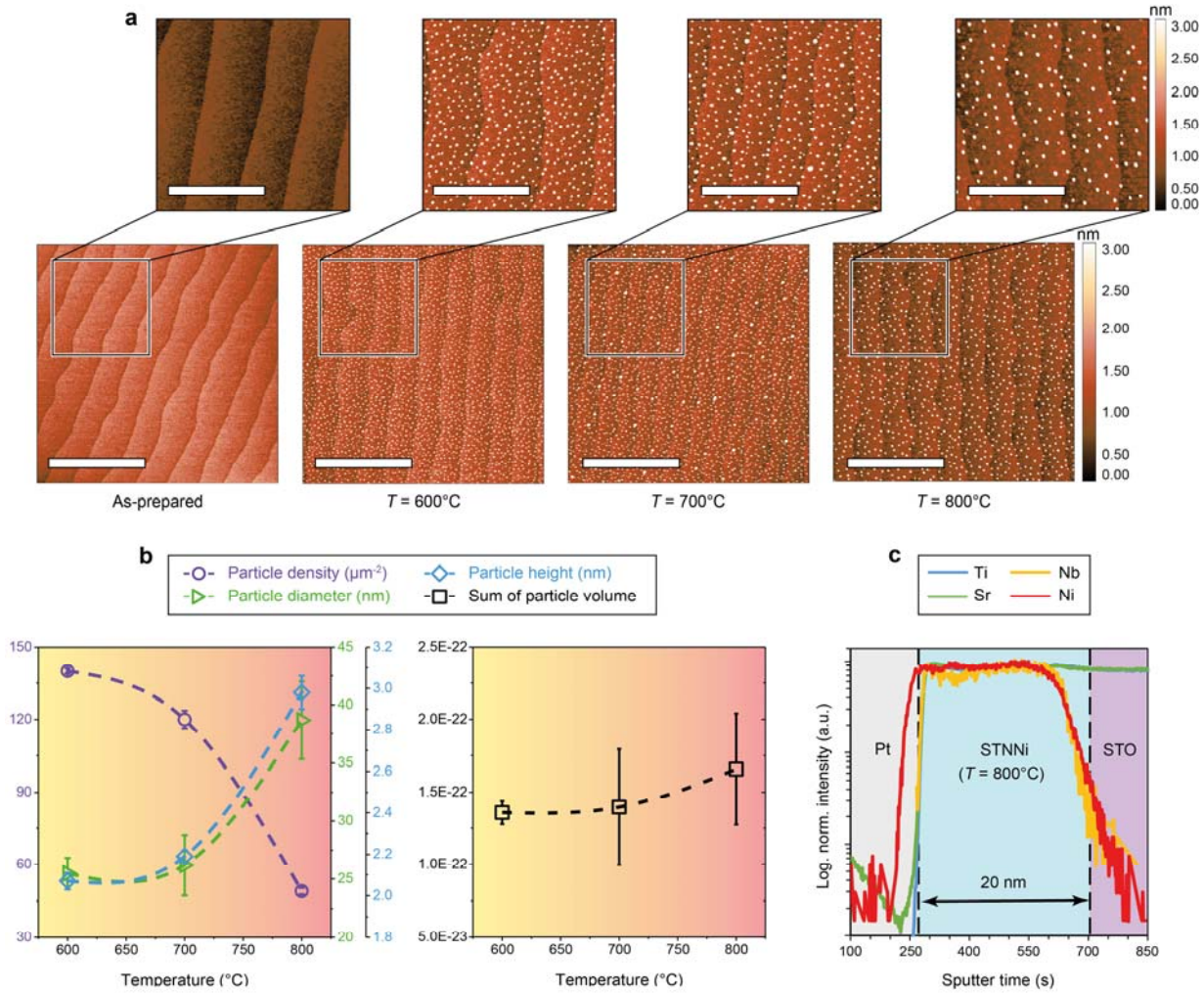

Fig. 1| Characterization of STNNi thin films deposited on STO with a thickness of 20 nm after reducing thermal treatment at different temperatures (4% H_2/Ar, t = 30 h). (a) Comparison of the surface morphology in the as-prepared state and after reducing treatment at T = 600°C, T = 700°C and T = 800°C. The AFM scan size is 5x5 µm^2 and scale bars 2 µm (below); 2x2 µm^2 and scale bars 1 µm (above) respectively. Decorations of the surface by exsolved nanoparticles are visible. (b) Nanoparticle properties determined based on the topological data showing averaged values obtained from three 5x5 µm^2 scans respectively. Error bars are based on standard deviations. While the particle density decreases, particle height and particle diameter increase with increasing temperature (left panel), the sum of the volume of the exsolved particles is similar after reduction at different temperatures (right panel). Note that solely the volume of the part of the particles penetrating the surface is detected. (c) Cation distribution determined by SIMS profiling of an STNNi sample covered with 30 nm of evaporated platinum after reduction at T = 800°C. Nickel accumulation can be observed at the surface, while the concentration appears to remain constant in the thin film bulk. Dashed lines serve as guide for the eye (b) and denote the Pt-to-thin film interface as well as the thin film-to-substrate interface (c).

A clear limitation of the dopant transport to the topmost surface region is evident in this system, where higher temperatures lead to coalescence of the nanoparticles, while exsolution from larger lengths scales is suppressed. Hence, only a small fraction of Ni-dopants present in the as-prepared STNNi thin films is

exsolved to the surface, while the Ni dopants predominantly remain buried in the perovskite bulk in the form of metallic particles.[17]

Probing surface space charge upon exsolution

To resolve the redox response at the STNNi surface, the chemical and electronic processes are probed by near-ambient pressure X-ray photoelectron spectroscopy (NAP-XPS). The spectroscopic signature is monitored *in-situ* during the exsolution process at a constant sample temperature, while the oxygen chemical potential is controlled by supply of oxygen and hydrogen gas. As discussed above, metal exsolution appears to be strongly limited to the surface region of the perovskite thin film (*cf.* Fig. 1), well-comparable to the typical screening lengths of space charge regions in highly doped oxides.[35,36] To investigate the formation of space charge regions (SCRs) and their influence on metal exsolution, XPS core-level spectra are recorded to compare two different measurement protocols.

We first investigate the redox chemistry during fast introduction of hydrogen into the XPS chamber (Fig. 2a, protocol 1). In a second measurement, we study the influence of an initial oxidizing thermal treatment, which is performed prior to the reducing annealing, on the exsolution response (Fig. 2a, protocol 2). We pay special attention to the spectroscopic changes visible in the Ni 2*p* region to track the evolution of a metallic Ni signature indicative for the formation of nanoparticles. In particular, we qualitatively follow the chemical state of nickel dopants based on the main peak of the complex Ni $2p_{3/2}$ core-level signal. For the as-prepared state, a peak centered at B.E. ~855.6 eV is visible (oxidized state) while the main peak of the metallic Ni $2p_{3/2}$ state is centered at B.E. ~851.9 eV.[37–39] Please note, that the absolute binding energy of the metal signal is influenced by the size of the supported nanoparticles and by interactions with the oxide support.[40–43] The spectra displayed in Fig. 2a were normalized to the pre-peak region. Notably, the intensity of the core-level signals is not quantitative due to the ongoing lateral separation of the material system during nanoparticle formation, which results in continuous changes in measurement geometry

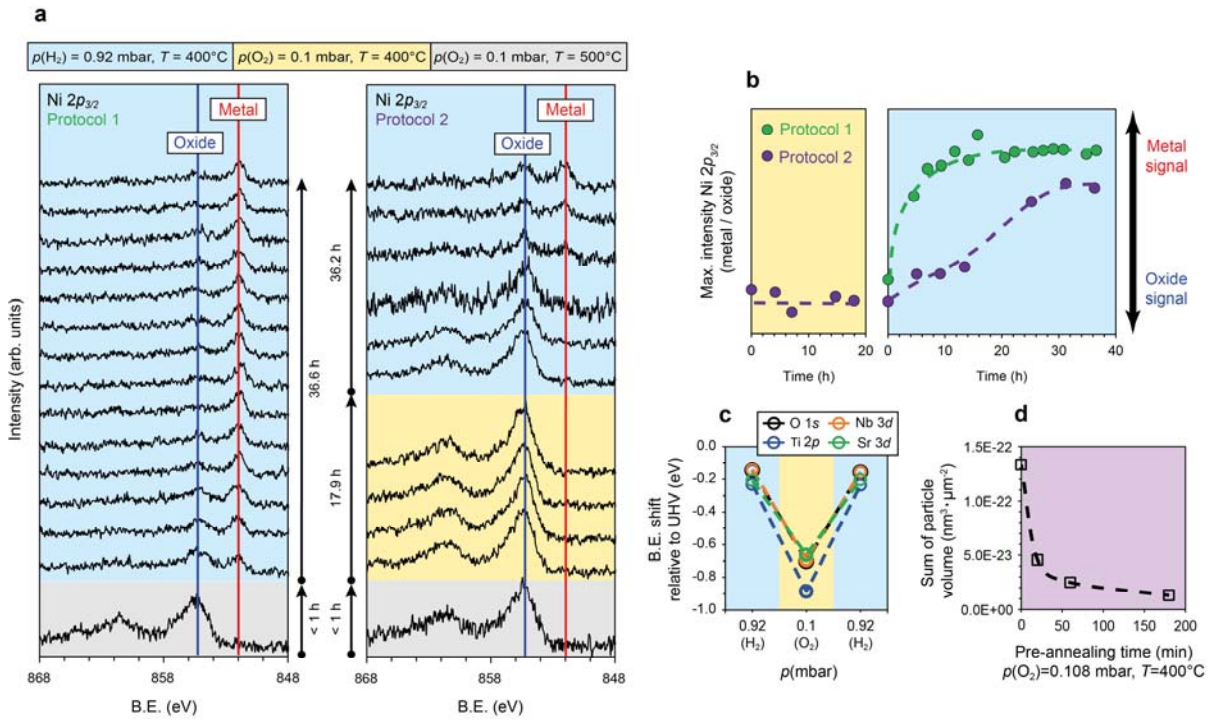

Fig. 2| Analysis of the interplay between redox chemistry of STNNi and nickel exsolution. (a) *In-situ* analysis of the Ni $2p_{3/2}$ core-level spectrum by near-ambient pressure X-ray photoelectron spectroscopy during reducing and oxidizing sample treatment at elevated temperatures using two different annealing protocols. Rapid formation of a metallic signature can be observed during reduction (protocol 1). In comparison, oxidizing pre-treatment of the STNNi thin films results in a considerably delayed redox response *i.e.* delayed formation of metallic nanoparticles (passivation effect) at the perovskite surface (protocol 2). The binding energies of all spectra were corrected to the Ti 2*p* position and the intensity was normalized to the pre-peak region. (b) Illustration of the exsolution dynamics during protocol 1 and protocol 2 based on the signal ratio of the metal and oxide feature. The evolution of a metallic Ni signal is strongly delayed after oxidizing pre-annealing performed during protocol 2. (c) Based on shifts in the binding energy relative to ultra-high-vacuum conditions, the formation of a surface space charge region can be observed. The space charge potential is different for oxidizing and reducing conditions as it depends on the respective electric and ionic reconstruction in the surface region. (d) *Ex-situ* studies of the surface passivation effect due to oxidizing pre-annealing show, that the delayed exsolution is directly correlated to a reduced particle volume as determined by microscopic investigations. The sample pieces were pre-annealed under oxidizing conditions for t = 20 min, t = 60 min and t = 180 min ($p(O_2)$ = 0.108 mbar, T = 400°C) and compared to an as-prepared sample after thermal reduction in the same process step (4%H_2/Ar, 400°C, t = 5 h). Dashed lines serve as guide for the eye. Sample conditions are denoted by the color code given above.

upon metal exsolution. However, the intensity ratio of the metal and oxide signals can be used to monitor the dynamics of nanoparticle formation at the perovskite surface.

As can be seen in Fig. 2a, b (protocol 1), the introduction of hydrogen results in a rapid formation of metallic Ni species at the thin film surface as indicated by the fast evolution of a metallic signal. The co-existence of Ni in the oxidized state is evident based on the presence of a (remaining) oxide signal of considerably reduced intensity as compared to the pristine state. Over time, the metallic signal is furthermore slightly increasing while the oxide signal in turn decreases during the reducing treatment.

149 In contrast, *in-situ* spectroscopy reveals no significant changes in the Ni surface chemistry during the initial
150 oxidizing treatment of STNNi (Fig. 2a, b; protocol 2). After holding the measurement conditions constant
151 for about t = 17.9 h, hydrogen is introduced into the chamber to induce the exsolution process.
152 Interestingly, the rapid exsolution response observed during protocol 1 remains absent for the oxidized
153 sample. More precisely, the exsolution of metallic nanoparticles to the perovskite surface is strongly
154 retarded. While a rapid evolution of a metallic signal was observed immediately after introduction of
155 hydrogen during protocol 1 (after t ~4.5 h), indications for the formation of a metallic signature during
156 protocol 2 are first visible after t ~25 hours of reduction (Fig. 2b).

157 Comparing the measurement protocols presented above, a clear passivation effect of the oxidizing
158 pre-treatment that delays the exsolution response is apparent. Complimentary morphologic studies of
159 STNNi samples were performed *ex-situ*, after pre-annealing at T = 400°C and at $p(O_2)$ = 0.108 mbar, which
160 is comparable to the conditions present during *in-situ* NAP-XPS investigations. With an increasing duration
161 of the oxidizing pre-annealing (t = 20 min, t = 60 min and t = 180 min), the subsequent reduction of the
162 thin film samples at T = 400°C under 4% H_2/Ar gas flow for t = 5 h results in striking differences of the
163 exsolved particle volume. As shown in Fig. 2d, the particle volume strongly decreases for samples which
164 have been oxidized before the reducing treatment (for AFM scans see Supplementary Fig. S3a), while the
165 sum of the exsolved particle volume determined for the sample which was not pre-oxidized is well
166 comparable to the volume obtained during long-term annealing at significantly higher temperatures and
167 longer annealing times presented above (*cf.* Fig. 1a, b). Here, even short pre-annealing times have a large
168 impact on the exsolution response of nickel induced during a comparably long reducing treatment of five
169 hours. Notably, the low pre-annealing temperatures kinetically suppress any significant changes of the
170 crystallographic properties of the bulk material, clearly indicating a surface process as the origin for the
171 observed passivation effect and in line with the findings discussed above. Accordingly, X-ray diffraction
172 analysis reveals no changes in the position of the thin film reflection after oxidizing treatment (*cf.*

Supplementary Fig. S3b). Importantly, no changes in the total Sr / Ti ratio is detected at the surface by our *in-situ* spectroscopy investigations over the course of the oxidizing annealing step of protocol 2 (*cf.* Supplementary Fig. S4a). A stoichiometric effect due to the formation of an extended blocking layer of different phase at the surface hence can be ruled out as the origin of the altered exsolution behaviour. Consistently, no significant surface roughening was observed upon oxidation (*cf.* Supplementary Fig. S4b,c).

Apart from the clear changes in the chemical state of Ni, more subtle changes can be observed in the signatures of the other elements, *i.e.* in the Ti 2*p*, Sr 3*d* Nb 3*d* and O 1*s* core-level spectra discussed in Supplementary Fig. S5. Prominent and uniform shifts in the binding energy of the core-level spectra of all elements, as well as broadening of the signals are evident in the different gas atmospheres. The shift in binding energy is plotted in reference to the peak position recorded in UHV (at room temperature) in Fig. 2c for oxidizing and reducing conditions, respectively. Since the spectra are obtained from the perovskite support, the evident shift in binding energy is not related to the nanoparticle size as observed for the metallic Ni 2*p* signal. The apparent peak shifts also cannot be understood in terms of sample charging due to insufficient supply of electrons from the thin film bulk. Such limited charge compensation would result in a continuous shift toward larger binding energies and for *n*-STO would be expected to be most pronounced in oxidizing conditions, whereas the observed shift upon oxidation is in the opposite direction. The magnitude of the shift in binding energy furthermore depends on the ambient reducing and oxidizing conditions and was shown to be related to the presence of space charge regions at the surface.[44–46] The formation of surface space charge regions is related to the inherent defect chemistry and the respective redox response of the material under different oxygen chemical potential.[44,47–49] Notably, the time-scale of the retarded exsolution response after oxidizing pre-annealing is very similar to the dynamic response of the space charge layer, detected for Nb-doped $SrTiO_3$ by electrical measurements.[45] Our observations hence indicate that the kinetics of Ni exsolution in STNNi is considerably affected by the presence of surface space charge.

The broadening of the NAP-XPS spectra may have different origins, some of which are directly related to the formation of SCRs at the surface. Here, peak broadening may be induced by the potential gradient at the surface[44,50,51], secondary phase formation as well as scattering effects with the ambient oxygen or hydrogen molecules. Remarkably, the apparent peak broadening is most pronounced for the Sr 3*d* region under oxidizing conditions, which results in a significantly flattened intensity valley in between the Sr 3*d* (Sr $3d_{5/2}$ and Sr $3d_{3/2}$) doublet. This observation may indicate the evolution of a minor SrO or $Sr(OH)_2$ surface phase, which is contributing to the signal in form of a second, superimposed doublet of slightly different binding energy. The formation of a Sr-rich surface phase under oxidizing conditions is a direct consequence of the defect chemistry of the perovskite host lattice and strongly entangled with the formation of surface space charge regions as well as the observed passivation effect. Notably, repeated cycling results in reversible and reproducible binding energy shifts accompanied by respective changes in the width of the photoemission signals (*cf.* Supplementary Fig. S5).[44,48,51]

The role of surface space charge regions for metal exsolution

To understand the nature of the surface space charge regions under oxidizing and reducing conditions and their influence on the exsolution process, the specific structural characteristics of the present material system have to be considered. As we have shown in our previous work, nickel dopants in STNNi thin films tend to accumulate in dopant-rich nanostructures rather than dissolve homogenously within the host lattice.[17] The Ni-rich clusters serve as centers for the nucleation of metallic nanoparticles in the thin film bulk. Thus, the host lattice is predominantly Nb-doped and follows the redox chemistry of donor-doped strontium titanate.

For Nb-doped $SrTiO_3$, surface space charge regions can be of two different kinds (Fig. 3a). Oxidizing treatment results in the annihilation of surface-near oxygen vacancies present in the perovskite host lattice. Additionally, to compensate the charge of donor-type dopants such as niobium, strontium vacancies accumulate, which are kinetically trapped in the surface region of the perovskite, as mediated

221 by the partial Schottky equilibrium.[44,47,48,52–54] In consequence, a negative space charge potential is
222 established at the perovskite surface (Fig. 3a, left), which results in a repulsive interaction for negatively
223 charged species, such as mobile acceptors (*e.g.* Ni in $SrTiO_3$), due to the gradient of the electrostatic
224 potential between surface and bulk. The negative potential hence reflects an energy barrier with blocking
225 character for negative charges. In contrast, thermal treatment at highly reducing conditions may widely
226 suppress the formation of Sr-vacancies while oxygen vacancies are generated, energetically trapped and
227 thus predominantly present in the surface region of the perovskite oxide (Fig. 3a, right).[24,29,47,55] Hence a
228 negative space charge potential is diminished during reducing treatment.[53,56] And, remarkably, even
229 indications for an inversion of the surface space charge were observed, which would result in a positive
230 charge at the surface and a sign change in the electrostatic potential gradient.[47]

231 In Fig. 3b, we show simulated potential profiles of surface-near space charge regions depending on the
232 oxygen activity as determined by finite-element electrostatic space charge simulations, which cover a wide
233 range between oxidizing and highly reducing conditions. The kinetics of SCR formation is determined by
234 the species of lowest mobility *i.e.*, diffusion of Sr vacancies in oxidizing conditions, which at low
235 temperature is limited solely to the surface. At T = 400°C the formation of a negative space charge region
236 occurs during annealing at oxygen activities down to $a(O_2)$~10^{-40}, while the inversion towards a positive
237 SCR requires highly reducing conditions. At an oxygen activity of $a(O_2)$~10^{-50} (comparable to the oxygen
238 activity present in hydrogen during our experiments) the negatively charged blocking potential is fully
239 absent. Further decrease of the oxygen activity results in the establishment of a positive potential at the
240 perovskite surface. Notably the width of the space charge regions is comparably narrow at different
241 temperatures since the screening length is mainly determined by the (niobium) doping concentration. In
242 addition to the oxygen activity, the annealing temperature influences the electrostatic gradient present at
243 the oxide surface significantly (Fig. 3c).

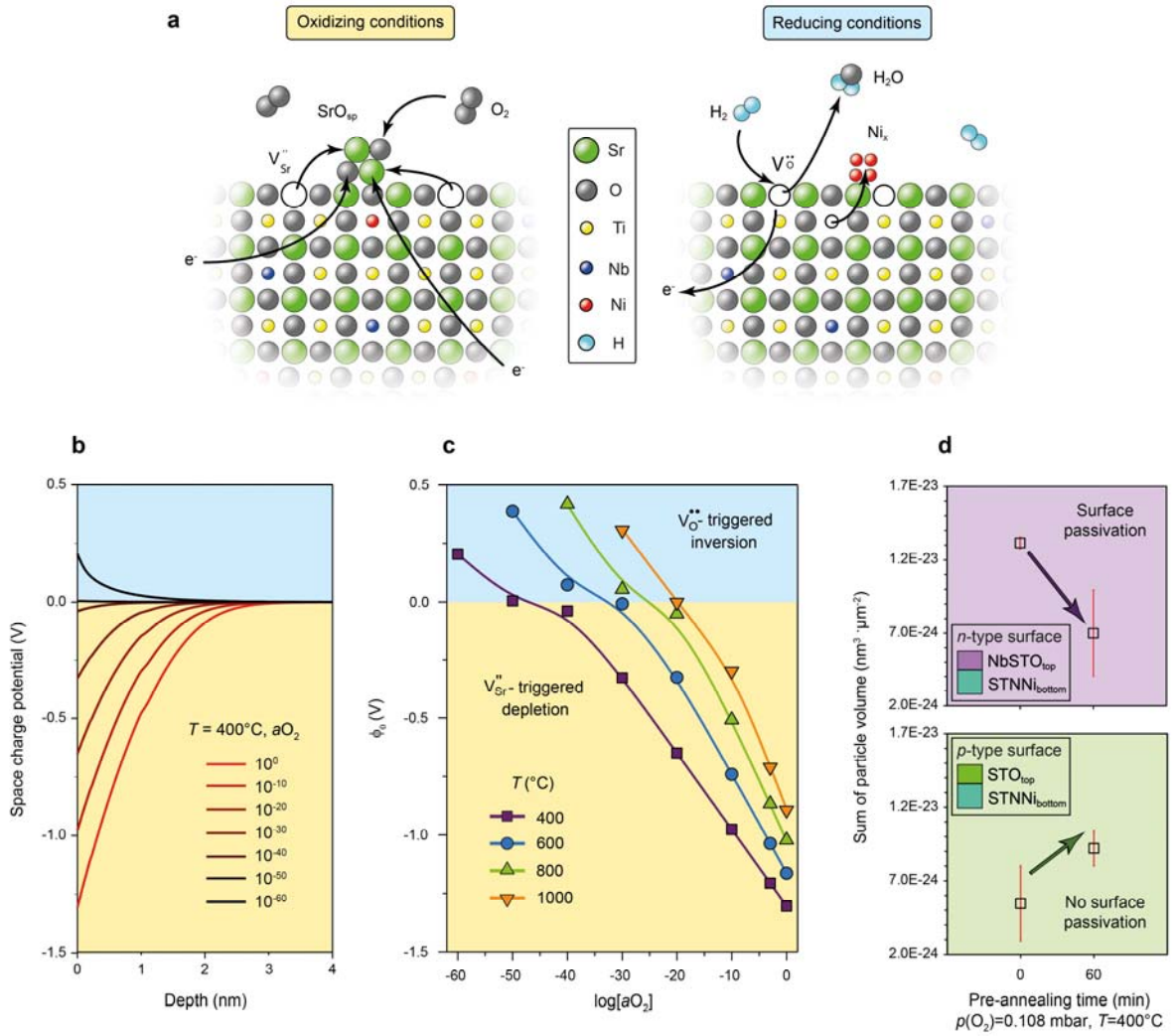

Fig. 3| (a) Simplified schematic illustration of the redox response of the STNNi host lattice and its impact on the diffusion of charged dopants (such as Ni'_{Ti}) to the surface. Negatively charged Sr vacancies are formed under oxidizing conditions, which are kinetically trapped in the near-surface region and hence a negative space charge potential is established. A positive space charge potential may be formed under highly reducing conditions by the generation of oxygen vacancies energetically trapped in the near-surface region. Kröger-Vink notation is used in the sketch. (b) Simulated potential profiles of space charge regions depending on the oxygen activity as determined by finite-element electrostatic space charge simulations for a temperature of T = 400°C. Negative surface space charge potentials result from thermal annealing in a wide range of oxygen activities. The magnitude of the space charge potential increases with decreasing oxygen activity. An inversion of the surface space charge towards a positive potential can be observed at very low oxygen activities. (c) Dependence of the space charge potential on the temperature and the oxygen activity. The temperature necessary to induce an inversion of the space charge potential increases with increasing oxygen activity. (d) Tailoring the surface redox chemistry to control the exsolution response of STNNi by deposition of a top layer with a thickness of four monolayers. Comparison of the exsolution response of STNNi with a top layer of donor-doped Nb:STO and undoped STO (naturally acceptor-doped by impurities). After an oxidizing thermal treatment is performed to activate the ionic sublattice of the top layer material (p(O2) = 0.108 mbar, T = 400°C, t = 60 min) before reduction (4% H_2/Ar, T = 600°C, t = 5 h), a clear influence of redox chemistry of the top layer material on the exsolution response is apparent. The nanoparticle volume is determined based on the topological data showing averaged values obtained from three 2x2 µm² scans respectively and error bars are based on standard deviations.

244 The inversion of the space charge potential observed in Fig. 3b,c indicates that only at extremely low oxygen

245 activity, the oxygen chemistry of STNNi governs the space charge and may even lead to an accelerated

246 exsolution response. The inversion of the space charge potential occurs at increasingly higher oxygen
247 activities with increasing temperature, although the blocking character caused by oxidation remains.

248 Since the redox response is determined by the redox chemistry of the topmost surface of the perovskite
249 and particularly the dopant concentration, slight modifications of the surface redox chemistry should
250 enable tailoring of the exsolution behaviour. For this purpose, epitaxial thin film samples are deposited in
251 so-called stack geometry, combining epitaxial STNNi with either a top layer of $SrTi_{0.95}Nb_{0.05}O_{3-\delta}$ (donor-
252 doped) or a top layer of nominally undoped $SrTiO_3$ (typically naturally acceptor-doped by
253 impurities.[24,29,48,57,58]

254 In this configuration, a lack of donor dopants close to the surface will suppress Sr vacancy formation and
255 thus the formation of a blocking surface depletion layer.[59,60] Only four monolayers of each Ni-free material
256 are epitaxially deposited on top of the exsolution-active STNNi bottom layer (20 nm), predominantly
257 changing the surface redox behaviour. Exsolution of Ni dopants through the originally Ni-free top layer is
258 visible after thermal reducing treatment (Supplementary Fig. S6). After thermal activation of the surface-
259 near ionic sublattice under oxidizing pre-annealing, however, the passivation effect for the donor-doped
260 surface becomes apparent in the form of a reduced volume of exsolved Ni nanoparticles (Fig. 3d). An
261 oxidizing treatment of the stack sample with an undoped top layer, however, does not result in surface
262 passivation. Here, the STO top layer determines the surface redox response of the stack sample.

263 Space charge regions are well-known to influence a wide range of properties in oxides and particularly in
264 functional ceramics.[19–34] For instance, electrostatic interactions of dopants with surface space charge
265 regions are known to promote the segregation of dopants during thermal treatment.[25] Space charge
266 regions also determine the grain boundary conductivity in ionically conducting ceramics.[61] Here, the nature
267 of the potential gradient, the charge of dopants and the defect chemistry of the host lattice are crucial for
268 the electrostatic interactions. Nickel dopants exhibit a negative charge relative to the B-site cations of the
269 host lattice Ti (IV) and Nb (V). Occupying the B-site of the perovskite structure, nickel-dopants are

expected to exhibit the nominal charge (III), while Ni-dopants present in form of NiO_x nanostructures (with $x \approx 1$)[17] are expected to have the nominal charge (II). Thus, at elevated temperatures and under oxidizing conditions, repulsive interactions of diffusing Ni ions with a negative surface space charge region can explain the observed surface passivation effect, resulting in a retarded exsolution response (Fig. 4, left panel). Such conditions are typically present during the synthesis of exsolution-active perovskites, with dopants accommodated within the oxide. The decrease of the negative space charge potential under reducing conditions results in a reduction of the blocking surface potential (Fig. 4, central panel). The solubility of Ni in the host matrix is considerably decreased at low oxygen pressures, resulting in the phase transition towards metallic nickel. Diffusive dopant transport of Ni ions in the surface region leads to accumulation of Ni-dopants in the form of nanoparticles at the surface. The reduction to metallic Ni at the surface causes a concentration gradient of nickel ions in the near-surface region, since the surface acts as a sink for Ni ions. In this way, the presence and strength of space charge regions at the surface can delay the exsolution response of the oxide.

An inversion of the space charge potential towards a positive surface charge under highly reducing conditions may even lead to attractive electrostatic interactions of Ni-dopants with the surface (Fig. 4, right panel). A positive surface charge region generated during reducing annealing and based on the enrichment of oxygen vacancies in the surface region consequently may serve as a gradient to further promote exsolution to the perovskite surface and to accelerate the kinetics of metal exsolution considerably. However, such extremely low oxygen activities are scarcely accessible under technically relevant conditions and the exsolution of acceptor-type dopants is expected to be mainly induced by the decrease of the blocking negative surface potential. Notably, thermodynamically derived parameters such as the enthalpy of oxygen vacancy formation will have an influence on the magnitude of the surface space charge potential and therefore may be a suitable lever to drive the surface potential into inversion and accelerate metal exsolution processes.

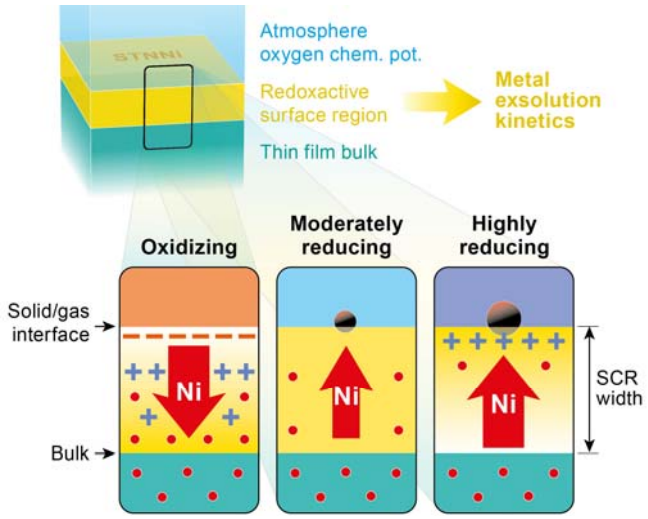

Fig. 4| Influence of surface space charge regions on metal exsolution kinetics at different oxygen chemical potentials, comparing oxidizing, moderately reducing and highly reducing conditions. In oxidizing conditions, a negative space charge potential is induced at the surface, which results in repulsive interaction with Ni-dopants of relative negative charge compared to the host cations. The magnitude of the space charge potential increases with decreasing oxygen activity *i.e.* under reducing conditions and allows for exsolution of Ni to the surface region, which serves as a sink of Ni dopants forming metallic nanoparticles. In consequence, a concentration gradient of Ni-dopants evolves which further promotes exsolution of dopants to the surface. At highly reducing conditions an inversion of the space charge region towards a positive surface potential may significantly promote the exsolution of dopants by attractive electrostatic interactions. The presence of surface-near SCRs is strongly entangled with the surface redox chemistry of the perovskite host lattice and widely dictates the exsolution kinetics. The electrostatic gradient of the SCR, critical for the release of dopants to the perovskite surface, is mainly determined by oxygen activity and temperature during thermal treatment.

Furthermore, the reversibility, *i.e.* switchability of exsolution processes by alternating reduction and re-oxidation of exsolution catalysts may be limited due to the presence of SCRs. Rapid formation of a surface-near SCR under oxidizing conditions may alter the kinetics of the indiffusion of Ni dopants. This is of high importance for the application of exsolution-active materials in catalytic converters, which aims to make use of the switchability of the catalysts' based on dynamic exsolution and dissolution of nanoparticles and requires fast response to the chemical environment.[12] Here, the influence of surface space charge on the exsolution kinetics needs to be taken into account.

Besides electrostatic interactions, SCRs may have an influence on the exsolution response due to the decrease of oxygen mobility in the near-surface region associated with the redox chemistry of the host lattice. The oxygen vacancy concentration is typically low in primarily donor-doped $SrTiO_3$. Consequently, the oxygen transport is rather slow, in particular after oxidizing treatment accompanied by the annihilation

of oxygen vacancies. The kinetics of oxygen exchange - fundamentally driving the exsolution process *via* the equilibration of the oxygen chemical potential in the material and the external atmosphere - is hence decreased when a negative SCR is present in the surface region. The surface passivation is coupled to both cation redox chemistry and oxygen chemistry, which are strongly entangled *via* space charge formation in this case. Space charge hence determines the mass transport dynamics of exsolving metal species across the solid-gas interface, while additional parameters such as surface energy of the metal nanoparticles on the surface may control the subsequent size and distribution of the surface nanoparticles.[12]

It is important to note that space charge formation at grain boundaries may also have a strong influence on the exsolution behaviour in ceramic materials.[24] Here, space-charge interactions may be associated to the preferential nucleation of nanoparticles along grain boundaries as reported in the literature.[62] Since space charge formation heavily depends on the local defect formation enthalpies close to the surface, orientation-dependent chemical composition and surface reconstructions[63] may have an influence on the nature of surface space charge regions formed at different crystallographic facets of powder grains[24,64,65] and hence need to be investigated to improve the understanding of metal exsolution processes in functional ceramics.

Since the enthalpy of formation for A-site vacancies in perovskites has a strong influence on the formation of space charge regions, it can be hypothesized that the chemical nature of the A-site ions has a strong influence on the exsolution of B-site dopants. Specifically, the well-documented enhancement of exsolution phenomena by A-site understoichiometry[5] may, at least in part, be related to modifications of the surface defect concentrations (and hence space charge regions) by the introduction of high concentrations of A-site vacancies in the bulk material.

CONCLUSION

We studied the redox response of exsolution-active and atomically-smooth STNNi thin films, mimicking the surfaces of single powder grains during controlled annealing procedures. We found a distinct passivation effect under oxidizing conditions, which is directly associated with the formation of a negative space charge region at the perovskite surface. We propose a mechanistic model for the transport of dopants to the perovskite surface, which is derived from our experimental and theoretical results. Here we show that electrostatic gradients present at the surface, which are determined by the redox chemistry of the perovskite surface, dictate the kinetics of metal exsolution processes. Surface passivation manifests in a significantly retarded exsolution response. Under reducing conditions, the equilibrium of the redox reaction shifts over time and the blocking potential decreases, allowing for the exsolution of acceptor-type dopants to the surface after an initial delay. In contrast, an inversion of the SCR towards a positive surface potential under strongly reducing conditions may even promote the exsolution kinetics and hence the formation of metallic nanoparticles at perovskite surfaces.

Surface space charge plays a key role in governing the functionality of exsolution materials. Here, the blocking character of surface space charge regions, which rapidly form under oxidizing conditions, may strongly influence the reversibility of metal exsolution, which is essential for regenerable catalysts for many material compositions. Electrostatic gradients at grain boundaries of ceramics furthermore will have considerable influence on the dopant transport pathways.

Tailoring the properties of surface space charge regions opens novel strategies for the rational design of exsolution materials. Here, control of the respective screening length *via* co-doping of the host lattice with elements which are stable under reducing conditions, may allow adjusting the dynamics of the exsolution response and the exsolution depth. As we have demonstrated, slight modifications of the redox chemistry of the topmost surface can be applied to heavily modify the exsolution response of doped perovskite

oxides, which opens new perspectives for the control of metal exsolution processes by surface and interface engineering.

METHODS

Epitaxy

Epitaxial $SrTi_{0.9}Nb_{0.05}Ni_{0.05}O_{3-\delta}$ (STNNi) thin films of 20 nm and 50 nm thickness were deposited with monolayer precision using reflection high-energy electron diffraction (RHEED)-controlled pulsed laser deposition (PLD) (Supplementary Fig. S1a). Please note that the experiments typically were performed using thin films of 20 nm thickness. Only when crystallographic properties were investigated (cf. Fig. 2d and Supplementary Fig. S3) thin films of 50 nm thickness were employed to allow for the investigation of a clearly separated thin film and substrate signal in X-ray diffraction (XRD). For PLD growth, single crystalline (001) $SrTiO_3$ and Nb:$SrTiO_3$ substrates (Shinkosha Co. Ltd., Yokohama, Japan) were applied (Supplementary Fig. S1b). For TiO_2-termination the substrates were etched in buffered HF and annealed at T = 950°C under continuous flow of an O_2/Ar (20/80) gas mixture for two hours. Nb-doped substrates were used when the analysis required a fully conductive sample. Thin film growth was performed at constant backside-temperature of T = 650°C using an IR-diode laser with a wavelength of λ = 925 nm for heating. A KrF excimer laser (Compex 205F, Coherent, Santa Clara, USA) operated with a repetition rate f = 5 Hz and with a wavelength of λ = 248 nm was applied for the ablation of the ceramic target material. The thin films were deposited at oxygen pressures of p(O2) = 0.108 mbar and using a laser fluence of F = 1.14 J·cm^{-2}. The thin film samples were immediately quenched to room temperature after the deposition was completed (no post-annealing). The ceramic STNNi target was prepared by cold isostatic pressing and subsequent sintering of a powder synthesized by the Pechini method. The target-to-substrate distance was d = 57 mm.

Thin film processing

Thermal treatment under reducing conditions (4% H_2/Ar) was applied to induce the exsolution process. After reducing thermal treatment, the thin film samples were quenched to room temperature under continuous gas flow.

Oxidizing pre-annealing was performed in the PLD chamber at an oxygen pressure of $p(O_2) = 0.108$ mbar and a temperature of $T = 400$°C using an IR-diode laser with a wavelength of $\lambda = 925$ nm for heating.

Thin film characterization

The surface morphology was characterized by atomic force microscopy (AFM; Cypher, Oxford Instruments Asylum Research Inc., Santa Barbara, USA) and the particle properties such as nanoparticle density, nanoparticle dimensions (median diameter and median height) and nanoparticle volume were determined from the topological data using the *Gwyddion* software. Crystallographic properties were investigated by X-ray diffraction (XRD) analysis in Bragg–Brentano geometry (D8 Discover, Bruker AXS GmbH, Karlsruhe, Germany). The diffractometer was equipped with a goebel mirror, a Cu K_α monochromator, a centric eulerian cradle, a lynxeye xe detector and a pinhole adapter (2 mm in diameter). Depth-profiling of the cation distribution (Ti^+, $^{86}Sr^+$, Ni^+, Nb^+ and Pt^+ signals) was performed by time-of-flight secondary ion mass spectrometry (ToF-SIMS_5.NCS, IONTOF GmbH, Münster, Germany) in negative polarity mode after 30 nm of platinum were evaporated at the sample surface.

***In-situ* spectroscopy**

In-situ analysis of the exsolution response was performed by custom-designed laboratory-based NAP-XPS (Specs Surface Nano Analysis GmbH, with monochromized Al-K_α source). To avoid charging effects during *in-situ* spectroscopy, conductive Nb-doped STO substrates were employed for the epitaxial growth of STNNi. The samples were fixed at the sample holder of the NAP-XPS system using metal stripes in order to ensure good electrical and thermal conductivity. Here, the K-type thermocouple was placed in between the sample surface and one of the metal stripes. Sample heating was realized by electron bombardment at the back of the sample stage while mounted on the NAP manipulator. The absolute binding energy scale was calibrated to the position of the Ti $2p_{3/2}$ core-level signal recorded under UHV conditions and at room temperature. XPS Ti 2*p*, Sr 3*d*, Ni 2*p*, Nb 3*d*, O 1*s* and C 1*s* core-level spectra were recorded during exposure of the samples to hydrogen or oxygen gas at a constant temperature of $T = 400$°C after a short heat-up of each sample to $T = 500$°C under oxygen atmosphere to remove carbon species adsorbed at the surface. The binding energy of all spectra displayed in Fig. 2a were corrected to the Ti 2*p* position (B.E. = 458.4 eV) and the intensity was normalized to the pre-peak region. No binding energy correction was performed for the core-level spectra displayed in the Supplementary Information. Typically, 50 scans were averaged

for each Ni 2*p* spectrum shown. In a few cases, a smaller number of scans is used owing to slight shifts in sample position over long probing durations, which resulted in a decreased signal-to-noise ratio of the signal over time. The core-level spectra were recorded with a pass energy of 20 eV, a step size of 0.05 eV, a dwell time of 200 ms and with a spectral resolution of 0.8 eV.

Finite-element electrostatic space charge simulations

Space charge calculations were based on bulk defect concentrations calculated for $SrTiO_3$ *via* band gap excitation, oxygen exchange reaction and dopant concentration. Space charge formation was calculated considering the dedicated surface defect reactions, comprising an active surface Schottky equilibrium (strontium vacancy formation[48]) as well as a reduced enthalpy of formation for oxygen vacancies in the most surface-near atomic layer.[24] As a result of the varied surface equilibria, surface defect concentrations differ from the expected bulk value, resulting in a redistribution of mobile defects and formation of a surface space charge layer, obeying electrostatic boundary conditions. Electrostatic potential, electric field and local defect concentrations were solved self-consistently using a finite-element routine, with the boundary condition of vanishing space charge in the bulk (global charge neutrality). $a{O_2}$-dependence was derived from the intrinsic $a{O_2}$-dependence of the defect equilibria. A detailed list of reaction equations and input parameters are given in the Supplementary Information (Supplementary Note 6).

REFERENCES

1. Hauch, A. *et al.* Recent advances in solid oxide cell technology for electrolysis. *Science* **370,** (2020).
2. Boldrin, P. & Brandon, N. P. Progress and outlook for solid oxide fuel cells for transportation applications. *Nat Catal* **2,** 571–577 (2019).
3. Davis, S. J. *et al.* Net-zero emissions energy systems. *Science* **360,** (2018).
4. Duan, C. *et al.* Highly durable, coking and sulfur tolerant, fuel-flexible protonic ceramic fuel cells. *Nature* **557,** 217–222 (2018).
5. Neagu, D., Tsekouras, G., Miller, D. N., Ménard, H. & Irvine, J. T. S. In situ growth of nanoparticles through control of non-stoichiometry. *Nature Chemistry* **5,** 916–923 (2013).
6. Neagu, D. *et al.* Nano-socketed nickel particles with enhanced coking resistance grown in situ by redox exsolution. *Nature Communications* **6,** 8120 (2015).
7. Kwon, O. *et al.* Exsolution trends and co-segregation aspects of self-grown catalyst nanoparticles in perovskites. *Nature Communications* **8,** 15967 (2017).
8. Han, H. *et al.* Lattice strain-enhanced exsolution of nanoparticles in thin films. *Nature Communications* **10,** 1471 (2019).
9. Opitz, A. K. *et al.* Understanding electrochemical switchability of perovskite-type exsolution catalysts. *Nature Communications* **11,** 4801 (2020).
10. Kim, J. H. *et al.* Nanoparticle ex-solution for supported catalysts: materials design, mechanism and future perspectives. *ACS Nano* **15,** 81–110 (2021).
11. Kwon, O., Joo, S., Choi, S., Sengodan, S. & Kim, G. Review on exsolution and its driving forces in perovskites. *J. Phys. Energy* **2,** 32001 (2020).
12. Nishihata, Y. *et al.* Self-regeneration of a Pd-perovskite catalyst for automotive emissions control. *Nature* **418,** 164–167 (2002).
13. Kousi, K., Tang, C., Metcalfe, I. S. & Neagu, D. Emergence and future of exsolved materials. *Small* (2021).

14. Ellingham. Transactions and Communications. *J. Chem. Technol. Biotechnol.* **63,** 125–160 (1944).

15. Gao, Y., Chen, D., Saccoccio, M., Lu, Z. & Ciucci, F. From material design to mechanism study: Nanoscale Ni exsolution on a highly active A-site deficient anode material for solid oxide fuel cells. *Nano Energy* **27,** 499–508 (2016).

16. Oh, T.-S. *et al.* Evidence and model for strain-driven release of metal nanocatalysts from perovskites during exsolution. *The journal of physical chemistry letters* **6,** 5106–5110 (2015).

17. Weber, M. L. *et al.* Exsolution of embedded nanoparticles in defect engineered perovskite layers. *ACS Nano* **15,** 4546-4560 (2021).

18. Gao, Y. *et al.* Energetics of nanoparticle exsolution from perovskite oxides. *The journal of physical chemistry letters* **9,** 3772–3778 (2018).

19. Ikeda, J. A. S. & Chiang, Y.-M. Space charge segregation at grain boundaries in titanium dioxide: I, relationship between lattice defect chemistry and space charge potential. *J American Ceramic Society* **76,** 2437–2446 (1993).

20. Shirpour, M. *et al.* Dopant segregation and space charge effects in proton-conducting $BaZrO_3$ perovskites. *J. Phys. Chem. C* **116,** 2453–2461 (2012).

21. Chiang, Y.-M. & Takagi, T. Grain-boundary chemistry of barium titanate and strontium titanate: I, high-temperature equilibrium space charge. *J American Ceramic Society* **73,** 3278–3285 (1990).

22. Chung, S.-Y., Choi, S.-Y., Yoon, H.-I., Kim, H.-S. & Bae, H. B. Subsurface space-charge dopant segregation to compensate surface excess charge in a perovskite oxide. *Angewandte Chemie* **55,** 9680–9684 (2016).

23. Yoon, H.-I. *et al.* Probing dopant segregation in distinct cation sites at perovskite oxide polycrystal interfaces. *Nature communications* **8,** 1417 (2017).

24. De Souza, R. A. The formation of equilibrium space-charge zones at grain boundaries in the perovskite oxide $SrTiO_3$. *Physical chemistry chemical physics: PCCP* **11,** 9939–9969 (2009).

25. Lee, W., Han, J. W., Chen, Y., Cai, Z. & Yildiz, B. Cation size mismatch and charge interactions drive dopant segregation at the surfaces of manganite perovskites. *Journal of the American Chemical Society* **135,** 7909–7925 (2013).

26. Waser, R. Electronic properties of grain boundaries in $SrTiO_3$ and $BaTiO_3$ ceramics. *Solid State Ionics* **75,** 89–99 (1995).

27. Sanna, S. *et al.* Enhancement of the chemical stability in confined δ-Bi_2O_3. *Nature materials* **14,** 500–504 (2015).

28. Korte, C., Peters, A., Janek, J., Hesse, D. & Zakharov, N. Ionic conductivity and activation energy for oxygen ion transport in superlattices—the semicoherent multilayer system YSZ (ZrO_2 + 9.5 mol% Y_2O_3)/Y_2O_3. *Physical chemistry chemical physics: PCCP* **10,** 4623–4635 (2008).

29. Gunkel, F. *et al.* Space charges and defect concentration profiles at complex oxide interfaces. *Phys. Rev. B* **93,** 245431 (2016).

30. Guo, X., Sigle, W. & Maier, J. Blocking grain boundaries in yttria-doped and undoped ceria ceramics of high purity. *J American Ceramic Society* **86,** 77–87 (2003).

31. Tuller, H. L., Litzelman, S. J. & Jung, W. Micro-ionics: next generation power sources. *Physical chemistry chemical physics: PCCP* **11,** 3023–3034 (2009).

32. Tuller, H. Ionic conduction in nanocrystalline materials. *Solid State Ionics* **131,** 143–157 (2000).

33. Taibl, S., Fafilek, G. & Fleig, J. Impedance spectra of Fe-doped $SrTiO_3$ thin films upon bias voltage: inductive loops as a trace of ion motion. *Nanoscale* **8,** 13954–13966 (2016).

34. Baiutti, F. *et al.* High-temperature superconductivity in space-charge regions of lanthanum cuprate induced by two-dimensional doping. *Nature Communications* **6,** 8586 (2015).

35. Ohtomo, A. & Hwang, H. Y. Surface depletion in doped $SrTiO_3$ thin films. *Appl. Phys. Lett.* **84,** 1716–1718 (2004).

36. Tanaka, H. *et al.* Nondestructive estimation of depletion layer profile in Nb-doped $SrTiO_3$/(La,Ba)MnO_3 heterojunction diode structure by hard x-ray photoemission spectroscopy. *Appl. Phys. Lett.* **98,** 133505 (2011).

37. Biesinger, M. C. *et al.* Resolving surface chemical states in XPS analysis of first row transition metals, oxides and hydroxides: Cr, Mn, Fe, Co and Ni. *Applied Surface Science* **257,** 2717–2730 (2011).

38. Payne, B. P., Biesinger, M. C. & McIntyre, N. S. Use of oxygen/nickel ratios in the XPS characterisation of oxide phases on nickel metal and nickel alloy surfaces. *Journal of Electron Spectroscopy and Related Phenomena* **185,** 159–166 (2012).

39. Biesinger, M. C., Payne, B. P., Lau, L. W. M., Gerson, A. & St. Smart, R. C. X-ray photoelectron spectroscopic chemical state quantification of mixed nickel metal, oxide and hydroxide systems. *Surf. Interface Anal.* **41,** 324–332 (2009).

40. Mason, M. G. Electronic structure of supported small metal clusters. *Phys. Rev. B* **27,** 748–762 (1983).

41. Wertheim, G. K. Core-electron binding energies in free and supported metal clusters. *Z. Physik B - Condensed Matter* **66,** 53–63 (1987).

42. Wertheim, G. K. Electronic structure of metal clusters. *Z Phys D - Atoms, Molecules and Clusters* **12,** 319–326 (1989).

43. Richter, B., Kuhlenbeck, H., Freund, H. J. & Bagus, P. S. Cluster core-level binding-energy shifts: the role of lattice strain. *Phys. Rev. Lett.* **93,** 26805 (2004).

44. Andrä, M. *et al.* Chemical control of the electrical surface properties in donor-doped transition metal oxides. *Phys. Rev. Materials* **3** (2019).

45. Andrä, M. *et al.* Oxygen partial pressure dependence of surface space charge formation in donor-doped $SrTiO_3$. *APL Materials* **5,** 56106 (2017).

46. Andrä, M. *et al.* Effect of cationic interface defects on band alignment and contact resistance in metal/oxide heterojunctions. *Adv. Electron. Mater.* **6,** 1900808 (2020).

47. Lewin, M. *et al.* Nanospectroscopy of infrared phonon resonance enables local quantification of electronic properties in doped $SrTiO_3$ ceramics. *Adv. Funct. Mater.* **28,** 1802834 (2018).

519 48. Meyer, R., Zurhelle, A. F., De Souza, R. A., Waser, R. & Gunkel, F. Dynamics of the metal-insulator transition of
520 donor-doped $SrTiO_3$. *Phys. Rev. B* **94** (2016).

521 49. De Souza, R. A., Metlenko, V., Park, D. & Weirich, T. E. Behavior of oxygen vacancies in single-crystal $SrTiO_3$:
522 equilibrium distribution and diffusion kinetics. *Phys. Rev. B* **85** (2012).

523 50. Chambers, S. A., Du, Y., Comes, R. B., Spurgeon, S. R. & Sushko, P. V. The effects of core-level broadening in
524 determining band alignment at the epitaxial $SrTiO_3$ (001)/ p-Ge(001) heterojunction. *Appl. Phys. Lett.* **110,** 82104
525 (2017).

526 51. Rose, M.-A. *et al.* Identifying ionic and electronic charge transfer at oxide heterointerfaces. *Adv. Mater.* **33,**
527 (2021).

528 52. Gunkel, F. *et al.* Influence of charge compensation mechanisms on the sheet electron density at conducting
529 $LaAlO_3$ /$SrTiO_3$ -interfaces. *Appl. Phys. Lett.* **100,** 52103 (2012).

530 53. Moos, R. & Hardtl, K. H. Defect chemistry of donor-doped and undoped strontium titanate ceramics between
531 1000° and 1400°C. *J American Ceramic Society* **80,** 2549–2562 (1997).

532 54. Zurhelle, A. F., Christensen, D. V., Menzel, S. & Gunkel, F. Dynamics of the spatial separation of electrons and
533 mobile oxygen vacancies in oxide heterostructures. *Phys. Rev. Materials* **4** (2020).

534 55. Waser, R., Baiatu, T. & Hardtl, K.-H. dc Electrical degradation of perovskite-type titanates: II, single crystals. *J*
535 *American Ceramic Society* **73,** 1654–1662 (1990).

536 56. Muenstermann, R. *et al.* Correlation between growth kinetics and nanoscale resistive switching properties of
537 $SrTiO_3$ thin films. *Journal of Applied Physics* **108,** 124504 (2010).

538 57. Waser, R. Bulk Conductivity and defect chemistry of acceptor-doped strontium titanate in the quenched state. *J*
539 *American Ceramic Society* **74,** 1934–1940 (1991).

540 58. Metlenko, V. *et al.* Do dislocations act as atomic autobahns for oxygen in the perovskite oxide $SrTiO_3$? *Nanoscale*
541 **6,** 12864–12876 (2014).

59. Kozuka, Y., Hikita, Y., Bell, C. & Hwang, H. Y. Dramatic mobility enhancements in doped $SrTiO_3$ thin films by defect management. *Appl. Phys. Lett.* **97,** 12107 (2010).

60. Inoue, H. *et al.* Delta-doped $SrTiO_3$ top-gated field effect transistor. *Appl. Phys. Lett.* **114,** 231605 (2019).

61. Parras, J. P. *et al.* The grain-boundary resistance of CeO_2 ceramics: A combined microscopy-spectroscopy-simulation study of a dilute solution. *J American Ceramic Society* **103,** 1755–1764 (2020).

62. Qi, H. *et al.* Reversible in-Situ exsolution of Fe catalyst in $La_{0.5}Sr_{1.5}Fe_{1.5}Mo_{0.5}O_{6-\delta}$ anode for SOFCs. *ECS Trans.* **91,** 1701–1710 (2019).

63. Sokolović, I. *et al.* Does a pristine, unreconstructed $SrTiO_3$ (001) surface exist?. eprint 2012.08831, (2020).

64. Zagonel, L. F. *et al.* Orientation-dependent work function of in situ annealed strontium titanate. *Journal of physics. Condensed matter: an Institute of Physics journal* **21,** 314013 (2009).

65. Kim, K. J. *et al.* Facet-dependent in situ growth of nanoparticles in epitaxial thin films: the role of interfacial energy. *Journal of the American Chemical Society* **141,** 7509–7517 (2019).